Journal of Controlled Release 386 (2025) 114082

Contents lists available at ScienceDirect

Journal of Controlled Release

journal homepage: www.elsevier.com/locate/jconrel

Structural characterization of mRNA lipid nanoparticles (LNPs) in the presence of mRNA-free LNPs

Xiaoxia Chen [a,b,c,1], Yongfeng Ye [b,c,1], Mengrong Li [b,c,1], Taisen Zuo [d,e], Zhenhua Xie [d,e], Yubin Ke [d,e], He Cheng [d,e], Liang Hong [b,c,f,g,*], Zhuo Liu [a,b,f,g,*]

[a] Department of Biochemistry and Molecular Biology, School of Basic Medical Sciences, Harbin Medical University, Harbin 150086, China
[b] Institute of Natural Sciences, Shanghai Jiao Tong University, Shanghai 200240, China
[c] School of Physics and Astronomy, Shanghai Jiao Tong University, Shanghai 200240, China
[d] Spallation Neutron Source Science Center, Dongguan 523803, China
[e] Institute of High Energy Physics, Chinese Academy of Sciences, Beijing 100049, China
[f] Shanghai National Centre for Applied Mathematics (SJTU Center), MOE-LSC, Shanghai Jiao Tong University, Shanghai 200240, China
[g] Zhangjiang Institute for Advanced Study, Shanghai Jiao Tong University, Shanghai 201203, China

ARTICLE INFO

Keywords:
mRNA lipid nanoparticles
mRNA-free LNPs
Small angle neutron scattering
Nano flow cytometry

ABSTRACT

Lipid nanoparticles (LNPs) have emerged as a versatile platform for mRNA delivery across a range of applications, including disease prevention, cancer immunotherapy, and gene editing. Structural models of mRNA lipid nanoparticles (mRNA-LNPs) have also been proposed based on characterization of samples by using various advanced techniques. Among these, small angle neutron scattering (SANS) has proven essential for elucidating the lipid distribution within mRNA-LNPs, a factor crucial to both their preparation and efficacy. However, recent findings suggest that the mRNA-LNP samples prepared via commercial microfluidic techniques may contain a substantial fraction of mRNA-free LNPs, casting doubt on the validity of earlier structural models. In this study, we employed contrast variation SANS to characterize both mRNA-free LNPs and our mRNA-LNP sample, and quantified the proportion of mRNA-free LNPs present to be ~30 % in our mRNA-LNP sample using nano flow cytometry. By removing the contributions of mRNA-free LNPs from the SANS data of our mRNA-LNP sample, we were able to precisely characterize the structure of mRNA-loaded LNPs. Consequently, we proposed structural models for both mRNA-free and mRNA-loaded LNPs. Notably, our analysis revealed similar lipid distributions and shell thicknesses between the two particle types, while the solvent content in mRNA-loaded LNPs was significantly higher, leading to a larger core size. This work not only offers a method for accurately characterizing the structure of mRNA-loaded LNPs, but also establishes criteria for selecting appropriate analytical techniques based on the structural parameters of interest. Therefore, our findings hold significant implications for the mechanistic understanding and quality control of mRNA-based vaccines.

1. Introduction

Lipid nanoparticles (LNPs) have proven to be versatile nanocarriers for delivering nucleic acids in a range of medical applications, including cancer immunotherapy (1,2), metabolic regulation (3,4), and prophylactic interventions (5,6). A typical LNP formulation comprises a cationic ionizable lipid, a helper lipid, cholesterol, and a PEGylated lipid, each contributing uniquely to the stability, structure, encapsulation efficiency, and in vitro and in vivo interactions (7,8). Specifically, the internal structure and surface morphology of nucleic acid-loaded LNPs vary with lipid composition, leading to differences in stability and therapeutic efficacy (9–12). To optimize the delivery of nucleic acids via LNPs, extensive structural characterizations have been conducted on small interfering RNA (siRNA)-containing LNPs (13–17), mRNA-containing LNPs (mRNA-LNPs) (12,13,18–20), and plasmid DNA-loaded LNPs (21,22) using advanced techniques such as cryogenic

* Corresponding authors at: Department of Biochemistry and Molecular Biology, School of Basic Medical Sciences, Harbin Medical University, Harbin 150086, China (Z. Liu); Institute of Natural Sciences, Shanghai Jiao Tong University, Shanghai 200240, China (L. Hong).
E-mail addresses: hongl3liang@sjtu.edu.cn (L. Hong), liuzhuo_jude@126.com (Z. Liu).
[1] These authors contributed equally: Xiaoxia Chen, Yongfeng Ye, Mengrong Li.

https://doi.org/10.1016/j.jconrel.2025.114082
Received 20 February 2025; Received in revised form 22 July 2025; Accepted 30 July 2025
Available online 31 July 2025

electron microscopy (cryo-EM) (14,15,18), nuclear magnetic resonance (NMR) (13,14,23), small angle X-ray scattering (SAXS) (12,14,22,24,25), and small angle neutron scattering (SANS) (12,21,22,26,27), etc. (16,17,19,20). These analyses have informed the development of structural models (12–14,17,19,21–23,26), which are critical for understanding the mechanisms of LNP mediated nucleic acid delivery and guiding the rational design of more effective LNPs (10,28–30).

As the four lipid components used to formulate lipid nanoparticles (LNPs) are primarily composed of similar elements—carbon, hydrogen, oxygen, and nitrogen—it is experimentally challenging to distinguish among them and accurately resolve their spatial distributions within the nanoparticle. Isotope contrast variation small angle neutron scattering (SANS), however, offers a solution by exploiting the differences in neutron scattering length density between hydrogen and deuterium (31). For instance, M. Y. Arteta and collaborators successfully used contrast variation SANS to elucidate lipid distributions, water content, and mRNA copy number within a single LNP (12,26). Similarly, Z. Li et al. utilized SANS to investigate acidification induced structural changes in plasmid DNA-loaded LNPs (21). It is worth noting that previous SANS analyses assumed a homogeneous payload distribution within LNPs, disregarding the possible presence of mRNA-free LNPs (12,21,26,27,32). This assumption is reasonable for siRNA-loaded LNPs, where each LNP typically encapsulates hundreds of siRNA molecules (16,17,33). For mRNA-LNPs encapsulating transcripts of more than 1000 nucleotides, the presence of mRNA-free LNPs may be substantial and should not be overlooked. S. Li et al. (20) and T. Sych et al. (34) reported that 40 % to 80 % of LNPs were devoid of mRNA cargo. More recently, Münter et al. (35) employed single-particle fluorescence microscopy to quantify mRNA encapsulation and reported a considerably lower proportion of mRNA-free LNPs (~12.1 ± 2.0 %). However, as discussed in a perspective by Simonsen (36), this assay may systematically underestimate the true fraction of mRNA-free particles due to limitations in detection sensitivity. Complementary studies by Geng et al. (37) using nano flow cytometry demonstrated that the proportion of mRNA-free LNPs can range from 13.0 % to 32.7 %, depending on the specific ionizable lipid used and preparation method. Collectively, these findings underscore that mRNA-free LNPs are a prevalent and variable component in mRNA-LNP formulations. This variability presents a significant challenge for structural characterization using ensemble techniques such as SANS and raises concerns about the generalizability of previously proposed structural models that did not account for the presence of mRNA-free particles (12,26,27,32). This issue has begun to gain recognition within the field. Gilbert et al. (22) applied distinct structural models to interpret SAXS data for both mRNA-free and mRNA-loaded LNPs, aiming to elucidate the redistribution of lipids during formulation and the subsequent dialysis process. In their SANS analysis of nucleic acid-loaded LNPs, the authors incorporated a combined model comprising a core–shell sphere and an additional broad peak centered around 1 nm^{-1} to represent internal structural features (22). Notably, this model assumes that the lipid distribution and water content are equivalent in both mRNA-free and mRNA-loaded LNPs. However, this assumption diverges from the structural interpretation proposed by Unruh et al. (24), who emphasized that mRNA-free and mRNA-loaded LNPs exhibit distinct internal water contents and structural organization. Importantly, even the structural information provided by Unruh et al. remains an average of mRNA-free and mRNA-loaded LNPs. Thus, the structural models derived from previous SANS studies warrant further re-evaluation in light of the significant proportion of mRNA-free LNPs in mRNA-LNP samples. As a consequence, several critical questions arise: What is the structural model of mRNA-free LNPs? How can we accurately resolve the structure of mRNA-loaded LNPs within a mixture that includes both mRNA-free and mRNA-loaded LNPs? Are the structures of mRNA-free LNPs and mRNA-loaded LNPs comparable, or do they differ substantially? Finally, can we reliably infer the structure of mRNA-loaded LNPs by examining the mixture of both types of particles, or does the presence of mRNA-free LNPs necessitate separate characterization to avoid structural misinterpretation?

To address the above questions, we encapsulated mRNA molecules containing 2856 nucleotides into lipid nanoparticles (LNPs) and determined that approximately 30 % of the LNPs in our mRNA-LNP sample were mRNA-free using nano flow cytometry (NanoFCM) (33,37). We then employed contrast variation very small angle neutron scattering (VSANS) to characterize both mRNA-free LNPs and our mRNA-LNP sample. A structural model of mRNA-free LNPs was constructed based on the measurement of the mRNA-free LNP sample. More importantly, we developed a method to isolate the structural information of mRNA-LNPs by subtracting the VSANS data of mRNA-free LNPs from the mRNA-LNP sample, accounting for the proportion of mRNA-free LNPs. Through fitting the VSANS data, we determined key structural parameters of mRNA-loaded LNPs, including lipid distribution, solvent content, and mRNA copy number per LNP, and constructed the corresponding structural model. As a result, we accurately quantified the proportions of mRNA-free LNPs and mRNA-loaded LNPs within the mRNA-LNP sample, and established distinct structural models for both particle types. Our findings offer a refined structural characterization of mRNA-LNP samples, taking into account for the presence of mRNA-free LNPs. This provides a more accurate model for mRNA-LNP samples, which has important implications for the mechanistic study and quality assessment of nucleic acid-loaded LNPs.

2. Results

2.1. Basic characterizations of the mRNA-free LNP and mRNA-LNP samples

In this study, we utilized a lipid formulation developed by Moderna, consisting of the ionizable cationic lipid SM-102, cholesterol, distearoylphosphatidylcholine (DSPC), and PEGylated lipid (DMG-PEG2000) in a molar ratio of 50:38.5:10:1.5 (5). This formulation, used in the COVID-19 mRNA vaccine, is well known for its efficiency in nucleic acid encapsulation and intracellular delivery. mRNA molecules containing 2856 nucleotides were encapsulated within this lipid formulation using a microfluidic technique (details in Materials and Methods). For comparison, a mRNA-free LNP sample was prepared using the same lipid formulation but without nucleic acids. As shown in Fig. 1a, the mRNA-LNP sample exhibits a larger particle size compared to the mRNA-free LNP sample, although both display similar size distributions. Cryogenic electron microscopy (cryo-EM) images (Figs. 1b, S1, and S2) reveal that most particles of mRNA-free LNPs and the mRNA-LNP sample exhibit bleb morphology, i.e., an approximately spherical but irregular structure with distinct electron density partitions. This bleb morphology of mRNA-LNPs has been reported in several previous studies (18,32,37–39), despite most structural studies on LNPs have focused on spherical particles (12,14,26,40). Interestingly, Cheng et al. demonstrated that, even with identical lipid compositions, different buffer systems can significantly influence the prevalence of bleb structures in LNPs (39). Specifically, they found that using 300 mM sodium citrate resulted in a high proportion of bleb-containing LNPs, whereas 25 mM sodium acetate yielded predominantly spherical particles with minimal blebbing. In our study, we prepared LNPs using 100 mM sodium citrate buffer, and the majority of our particles exhibited bleb-like morphology (Fig. 1b). These observations collectively suggest that buffer composition, particularly the concentration and type of counterions, is strongly correlated with bleb formation in LNPs. In addition to buffer effects, we acknowledge that several other factors have also been reported to influence bleb formation. For example, Leung et al. observed that replacing DSPC with DOPE in the helper lipid component suppressed bleb formation, yielding only spherical LNPs (38). Moreover, the nucleic acid payload itself appears to play a role; siRNA-loaded LNPs using the same lipid formulation did not exhibit bleb structures, whereas longer mRNA molecules did (38). Bleb formation has also been reported

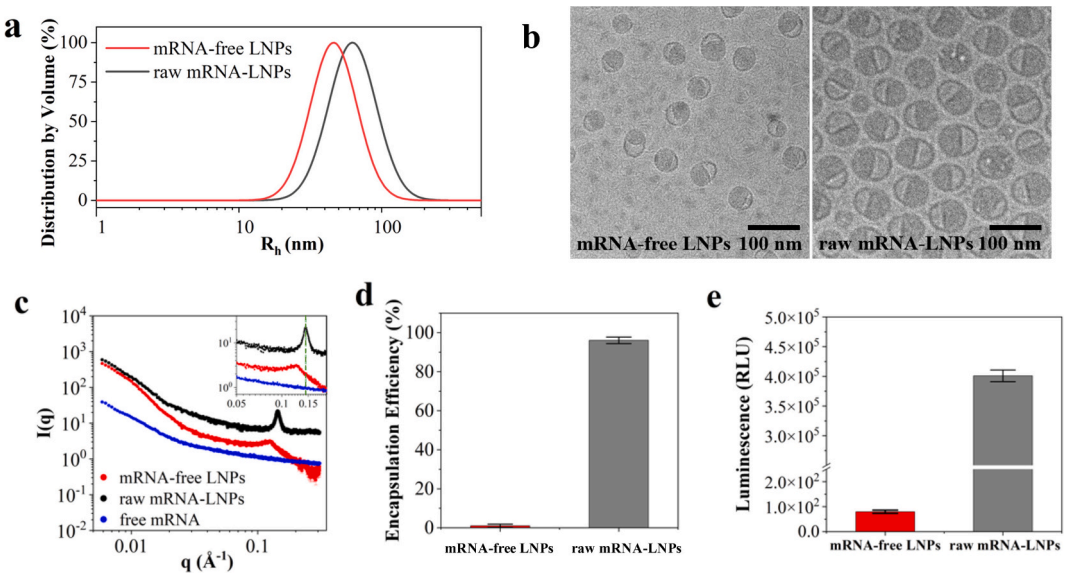

Fig. 1. Basic characterizations of the mRNA-free LNPs and our raw mRNA-LNP samples. (a) Particle size distributions, (b) cryo-EM images, (c) SAXS curves, (d) encapsulation efficiency, and (e) in vitro transfection potency of the mRNA-free LNPs and our raw mRNA-LNP samples. HEK293T cells were transfected by the mRNA-free LNPs and our raw mRNA-LNP samples. Luciferase expression was quantified after 24 h of incubation ($n = 3$).

as a result of post-processing conditions such as freeze-drying (18,41). Therefore, bleb morphology likely arises from a combination of factors, including lipid composition, buffer formulation, nucleic acid length, preparation method, and storage conditions (36). Based on the literature and our experimental observations, we suggest that the relatively high proportion of bleb-containing LNPs in our samples might be attributable to the use of 100 mM sodium citrate as the formulation buffer.

According to the electron density differences observed in the bleb particles, we propose that our mRNA-loaded LNPs are composed of a water-rich compartment and a lipid-rich compartment containing mRNA, consistent with the structural model proposed by Leung et al. (38). In a previous study, Brader et al. reported that mRNA localizes within the water-rich compartment of the core in their mRNA-LNPs (18). This conclusion was supported by cryo-TEM images showing mottled electron density within the aqueous compartment. Furthermore, thionine staining of non-spherical LNPs revealed enhanced contrast in the same region, reinforcing the assignment of the mottled density to encapsulated mRNA. In contrast, our cryo-TEM images reveal that the water-rich compartment in our mRNA-LNPs exhibits electron density similar to that of the surrounding aqueous medium, regardless of whether thionine is applied (Fig. S3a and S3b). This suggests that the mRNA is not located in the water-rich compartment but rather within the lipid-rich region of the core. To further probe the internal structure, we performed small-angle X-ray scattering (SAXS) on mRNA-free LNPs, raw mRNA-LNP samples, and free mRNA in aqueous solution. As shown in Fig. 1c, the SAXS curve for the mRNA-LNP sample presents a pronounced peak at $q \sim 0.13$ Å^{-1}, corresponding to a correlation distance of approximately 5 nm, which is much smaller in the mRNA-free LNPs. This result aligns with previous studies (12), where a peak around $q \sim 0.1$ Å^{-1} was attributed to the characteristic distance between mRNA molecules embedded in a lipid matrix. Furthermore, no such peak is observed in the SAXS profile of an aqueous mRNA solution (Fig. 1c) (32), confirming that the signal arises from lipid–mRNA interactions rather than free mRNA in solution. Taken together, the cryo-TEM and SAXS data strongly support a structural model in which mRNA is located within the lipid-rich compartment of the core in our mRNA-loaded LNPs. This contrasts with models proposed in other studies (18,32,39), where bleb morphology was attributed to the presence of mRNA in a distinct water-rich compartment alongside a lipid-rich domain. Notably, Cheng et al. (39) prepared such blebs using 300 mM sodium citrate, whereas in our study, blebs with mRNA localized in the lipid-rich compartment were obtained using 100 mM sodium citrate. These results suggest that the buffer composition, particularly the citrate concentration, may influence both the bleb morphology and mRNA distribution. However, further systematic studies are necessary to validate this hypothesis. Furthermore, the radius of gyration (R_g) of both samples was calculated from the SAXS data (Fig. 1c) (38). The R_g values for mRNA-free LNPs and raw mRNA-LNPs are approximately 32.8 nm and 46.1 nm, respectively, while their hydrodynamic radii (R_h) are 47.8 ± 2.0 nm and 63.5 ± 0.6 nm. We further assessed the encapsulation efficiency and in vitro transfection potency of both samples (Fig. 1d and e), confirming the high quality and efficacy of our mRNA-LNP formulation.

2.2. Structural characterization of mRNA-free LNPs by VSANS

Lipid nanoparticles (LNPs) are reported to play dual roles in mRNA vaccines, serving as adjuvants to enhance efficacy (42) and as potential immunogens that may induce adverse effects (43). However, detailed structural characterizations of mRNA-free LNPs remain scarce. In this work, we applied contrast variation very small angle neutron scattering (VSANS) to characterize the structure of mRNA-free LNPs. The LNP samples contained partially deuterated d70-DSPC and d7-cholesterol, and were suspended in solvents with four distinct D_2O/H_2O ratios (30 %, 51 %, 67 %, and 100 % D_2O). The VSANS data were collected in a q range from 0.003 Å^{-1} to 0.2 Å^{-1}, enabling the investigation of lipid distributions within both the core and shell of the LNPs. By varying the degree of isotope contrast, we were able to selectively highlight different components of LNPs, facilitating a more precise determination of the structural arrangement and lipid distribution within the core and shell. This approach provides critical insight into the structural organization of mRNA-free LNPs, a previously unexplored area in the context of nucleic acid-loaded nanoparticle formulations.

Fig. 1b illustrates the morphological similarity between mRNA-free LNPs and raw mRNA-LNPs, both exhibiting a core-shell bleb structure. To model these structures, we applied a core-shell ellipsoid model (44) in SasView (https://www.sasview.org) to fit the VSANS curves. Notably, the LNP surface was modeled as a single shell comprising both the phospholipids and the lipid anchors of the PEGylated lipids. This approximation is justified by the negligible scattering contribution of the highly hydrated PEG layer, which is estimated to exhibit ~67 %

hydration in its brush conformation (45). To further assess whether an additional shell was necessary to account for the PEG corona, we conducted a preliminary analysis of the SANS profiles. The resulting pair distance distribution functions and scattering length density profiles supported the adequacy of the single-shell core–shell model (see Fig. S4). As shown in Fig. 2, this model incorporates five fitting parameters: the equatorial radius of the core (r_{equat}), the polar radius of the core (r_{polar}), the shell thickness (t_{shell}), the scattering length density of the core (SLD_{core}), and the scattering length density of the shell (SLD_{shell}). Given that VSANS measurements were performed in four distinct D_2O/H_2O solvent contrasts, we reduced the number of fitting parameters by fixing the r_{polar}/r_{equat} ratio. This ratio was estimated based on cryo-EM analysis of over one hundred mRNA-free LNPs and over one hundred raw mRNA-LNPs. The values of r_{polar}/r_{equat} centered around ~1.2, with a standard deviation of ±0.1 for both sample types. Thus, we fixed the aspect ratio at 1.2 for model fitting, representing the average morphology observed across the LNP populations. Furthermore, we approximated the lipid-rich compartment inside the core to be spherical such that the volume fractions of water-rich and lipid-rich compartments in the core are 0.2/1.2 and 1/1.2, respectively (see Fig. 2d). Consequently, the SLD of the lipid-rich compartment in the core can be calculated using the following relationship: $SLD_{core} = 0.2/1.2 \times SLD_{sol} + 1/1.2 \times SLD_{lipid\text{-}rich}$, where SLD_{sol} and $SLD_{lipid\text{-}rich}$ are the scattering length densities of the solvent and the lipid-rich compartment, respectively. For each sample, the core radii and shell thickness were constrained to be consistent across the four solvent contrasts, while the SLD values of the core and shell were allowed to vary independently for each contrast. The volume fractions of core and shell in the mRNA-free LNPs, along with the solvent content and lipid composition in both regions can be derived based on the fitting results. Further details regarding the VSANS data analysis are provided in the Materials and Methods section.

According to the structural information obtained from the VSANS data, we proposed a structural model for mRNA-free LNPs (Fig. 3). To validate our findings, we conducted additional SANS measurements using a different spectrometer in a q range of 0.005 $Å^{-1}$ to 0.6 $Å^{-1}$ at the China Spallation Neutron Source. As shown in Fig. S5, the data collected from both VSANS and SANS exhibit similar behavior within the overlapping q range. However, due to limited beam time, the SANS experiments were performed only in solvents with D_2O volume fractions of 30 %, 51 %, and 67 %. Despite this limitation, the consistency between the two datasets supports the robustness of our structural model.

2.3. The proportion of mRNA-free LNPs in the mRNA-LNP sample

To obtain the structural information of mRNA-LNPs, we need to figure out the proportion of mRNA-free LNPs in the mRNA-LNP sample, thereby we utilized nano flow cytometry (NanoFCM) to detect fluorescence and side scattering at the single nanoparticle level. Since the mRNA molecules were labeled with a fluorescent dye, both fluorescence and side scattering were observed for the raw mRNA-LNPs, while only side scattering was detected for mRNA-free LNPs (Figs. 4a and S6). This allowed us to quantify the proportion of mRNA-free LNPs in the mRNA-LNP sample, which was found to be 27.7 ± 4.0 %, consistent with previous studies using the same technique (37). Additionally, we calculated the number-average payload of our mRNA-LNPs to be 2.9 ± 0.1 mRNA molecules, each 2856 nucleotides in length (Fig. 4b). It is important to note that the number of nucleic acid molecules encapsulated in each LNP is highly dependent on their length. For shorter siRNA-containing LNPs, hundreds of siRNA molecules can be encapsulated within each LNP (16,17,33). For mRNAs with lengths of 1029 and 2839 nucleotides, the payloads were 2.80 ± 0.41 (20) and 2.7 ± 0.4 (27) per LNP, respectively. Therefore, it is expected that fewer than three mRNA molecules are encapsulated per LNP when the mRNA length exceeds 2000 nucleotides.

2.4. Structure of mRNA-loaded LNPs characterized by VSANS

To elucidate the structure of mRNA-loaded LNPs in the presence of mRNA-free LNPs, we collected VSANS data for the mRNA-LNP sample containing deuterated DSPC (d70-DSPC) and deuterated cholesterol (d7-cholesterol) in solvents with varying D_2O/H_2O ratios. Fig. 5 displays the VSANS profiles for the mRNA-LNP sample, composed of both mRNA-loaded LNPs and mRNA-free LNPs (red circles and lines). Building on prior analyses, we had already determined the VSANS data for mRNA-free LNPs (Fig. 3a) and estimated their proportion in the mRNA-LNP sample (~30 %). Using this information, we were able to subtract the contribution of mRNA-free LNPs from the VSANS data of the mixed mRNA-LNP sample, thereby isolating the structural signal of mRNA-loaded LNPs. For clarity, we denote the mRNA-LNP sample with mixed mRNA-free LNPs and mRNA-LNPs as raw mRNA-LNPs, while mRNA-containing LNPs in the mixed mRNA-LNP sample are denoted as

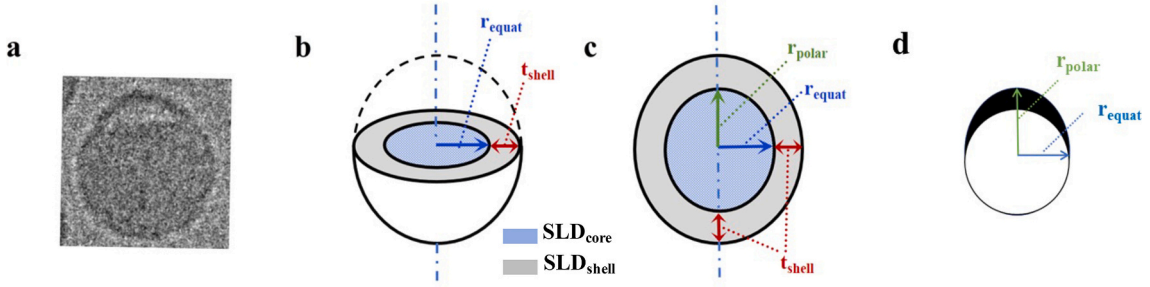

Fig. 2. Core-shell ellipsoid model for fitting mRNA-free LNPs and mRNA-loaded LNPs. (a) Representative cryo-EM image of mRNA-LNPs. (b-c) Schematic representation of a prolate ellipsoid used in the model. (d) Volume approximation of water-rich (black area) and lipid-rich (white area) compartments in the core. The diagram illustrates the geometric parameters: r_{equat}, r_{polar}, x_{core}, t_{shell}, SLD_{core}, and SLD_{shell} are equatorial radius of core, polar radius of core, ratio between equatorial radius and polar radius, thickness of shell, scattering length density of core, and scattering length density of shell, respectively. The blue and grey areas represent the scattering length density of the core (SLD_{core}) and the shell (SLD_{shell}) in panels b and c, respectively. Note that the lipid-rich compartment in the core is approximated to be spherical, thereby the volume of lipid-rich compartment is $V_{lipid-rich} = \frac{4}{3}*\pi*r_{equat}^3$. As the core is a prolate ellipsoid, the volume of the core is $V_{core} = \frac{4}{3}*\pi*r_{equat}^2*r_{polar}$, and the volume of the water-rich compartment is $V_{water-rich} = V_{core} - V_{lipid-rich} = \frac{4}{3}*\pi*r_{equat}^2*(r_{polar} - r_{equat})$. Consequently, the volume fraction of the lipid-rich compartment in the core is $vf_{lipid-rich} = V_{lipid-rich}/V_{core} = \left(\frac{4}{3}*\pi*r_{equat}^3\right)/\left(\frac{4}{3}*\pi*r_{equat}^2*r_{polar}\right) = r_{equat}/r_{polar}$, whereas the volume fraction of the water-rich compartment is $vf_{water-rich} = 1 - vf_{lipid-rich} = 1 - r_{equat}/r_{polar}$. In this study, we fixed the ratio of the equatorial to polar radius at 1.2 based on cryo-EM images of mRNA-free LNPs and mRNA-LNPs. Hence, the volume fractions of water-rich and lipid-rich compartments in the core are 0.2/1.2 and 1/1.2, respectively. (For interpretation of the references to colour in this figure legend, the reader is referred to the web version of this article.)

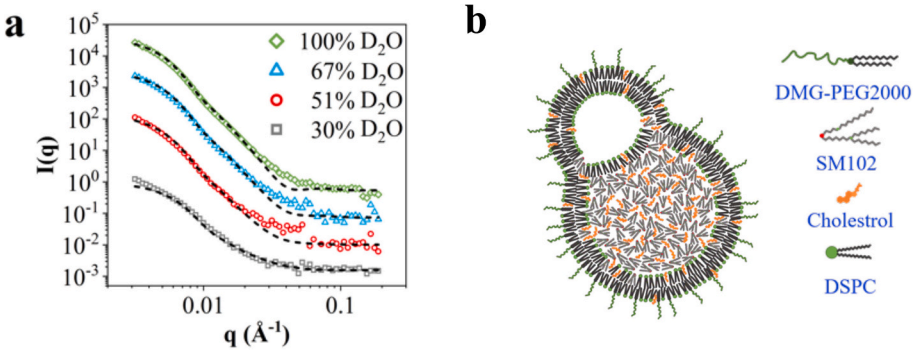

Fig. 3. Structural characterization of mRNA-free LNPs by VSANS. (a) VSANS data collected for mRNA-free LNPs in four different solvent contrasts: 30 % D_2O (grey squares), 51 % D_2O (red dots), 67 % D_2O (blue triangles), and 100 % D_2O (green diamonds). The black dash lines are the results of model fitting. (b) The structural model of mRNA-free LNPs proposed according to the VSANS fitting results. (For interpretation of the references to colour in this figure legend, the reader is referred to the web version of this article.)

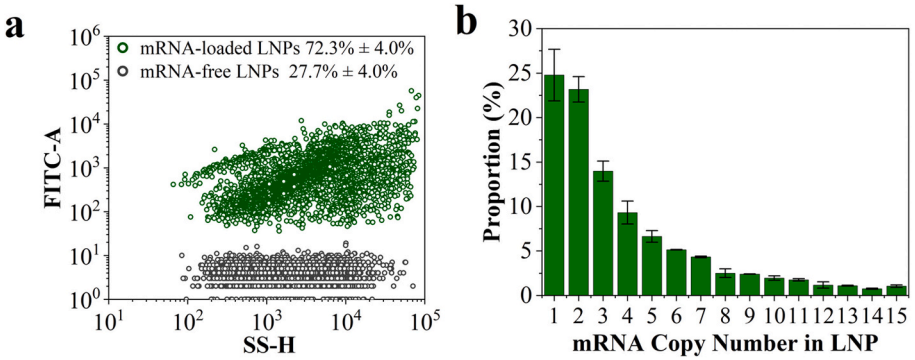

Fig. 4. Determination of the proportion of mRNA-free LNPs in the mRNA-LNP sample. (a) Compiled bivariate dot-plot of the FITC-A (fluorescence) burst area versus the SS (side scattering) burst area for mRNA-free LNPs (black circles) and mRNA-loaded LNPs (green circles). (b) The mRNA copy number distribution in the mRNA-loaded LNPs. The number-average payload of mRNA-loaded LNPs was calculated as the sum of the product of mRNA copy number per LNP and its corresponding population fraction. (For interpretation of the references to colour in this figure legend, the reader is referred to the web version of this article.)

mRNA-loaded LNPs. As depicted in Fig. 5, the VSANS data for mRNA-loaded LNPs exhibit a distinct profile from raw mRNA-LNPs across all solvent contrasts. Similar to our approach with mRNA-free LNPs, we fit the VSANS data of mRNA-loaded LNPs using a core-shell ellipsoid model. For consistency, we maintained the ratio of equatorial to polar radii at 1.2 and kept the radius and shell thickness constant across the different solvent contrasts. However, the scattering length densities (SLDs) of the core and shell were allowed to vary independently for each contrast. From the data fitting, we estimated the volume fractions of core and shell, as well as the solvent content and lipid composition within core and shell of mRNA-loaded LNPs, and compared these values to those of mRNA-free LNPs. Our analysis also indicated that the average number of mRNA molecules per LNP was 3.2 ± 0.2, in accordance with the payload determined by NanoFCM (Fig. 4b). A detailed description of the VSANS data analysis is provided in Materials and Methods. Based on the structural parameters obtained from the fitting, we propose a refined structural model for mRNA-LNPs (see Fig. 5e).

3. Discussion

While the structure of mRNA-LNP samples has been extensively investigated using small angle neutron scattering (SANS), the presence of mRNA-free LNPs within the mRNA-LNP samples has often been overlooked, potentially introducing bias into existing structural models. This oversight is particularly significant given that the proportion of mRNA-free LNPs in samples prepared via commercial microfluidic techniques can exceed 40 %. To obtain the accurate structural models, we conducted contrast variation very small angle neutron scattering (VSANS) on both mRNA-free LNPs and our mRNA-LNP sample. The mRNA-LNP sample is the mixture of both mRNA-free and mRNA-loaded LNPs, denoted as raw mRNA-LNPs in this study. In parallel, we quantified the proportion of mRNA-free LNPs in the raw mRNA-LNPs using nano flow cytometry (NanoFCM). By subtracting the contribution of mRNA-free LNPs from the VSANS data of raw mRNA-LNPs, we were able to isolate the structural data specific to mRNA-loaded LNPs. Here we denoted the LNPs encapsulated mRNA as mRNA-loaded LNPs to distinguish them with raw mRNA-LNPs. Structural parameters for both mRNA-free and mRNA-loaded LNPs were extracted using a core–shell ellipsoid model, with the corresponding schematic representations shown in Figs. 3b and 5e. Fig. 6 summarizes representative structural models previously reported for mRNA-loaded LNPs. These include a spherical model (26) (Fig. 6a) and a bleb model in which the mRNA is localized in the aqueous compartment (39) (Fig. 6b). In this work, we present a bleb model in which the mRNA resides within the lipid-rich compartment (Fig. 6c), consistent with the morphology observed in our cryo-EM images and supported by SAXS and SANS data analysis. This model aligns with previous report where macromolecular payloads were encapsulated in lipid-rich regions through controlled mixing techniques (38). Importantly, our approach also enables the structural resolution of mRNA-LNP samples containing both mRNA-free and mRNA-loaded LNPs, providing a more comprehensive view of particle heterogeneity.

Table 1 summarizes the structural parameters of our mRNA-free LNPs, mRNA-loaded LNPs, and raw mRNA-LNPs. For comparison, the structural parameters of raw mRNA-LNPs prepared by Sebastiani et al. (26) and Li et al. (27) are also included. While differences in mRNA

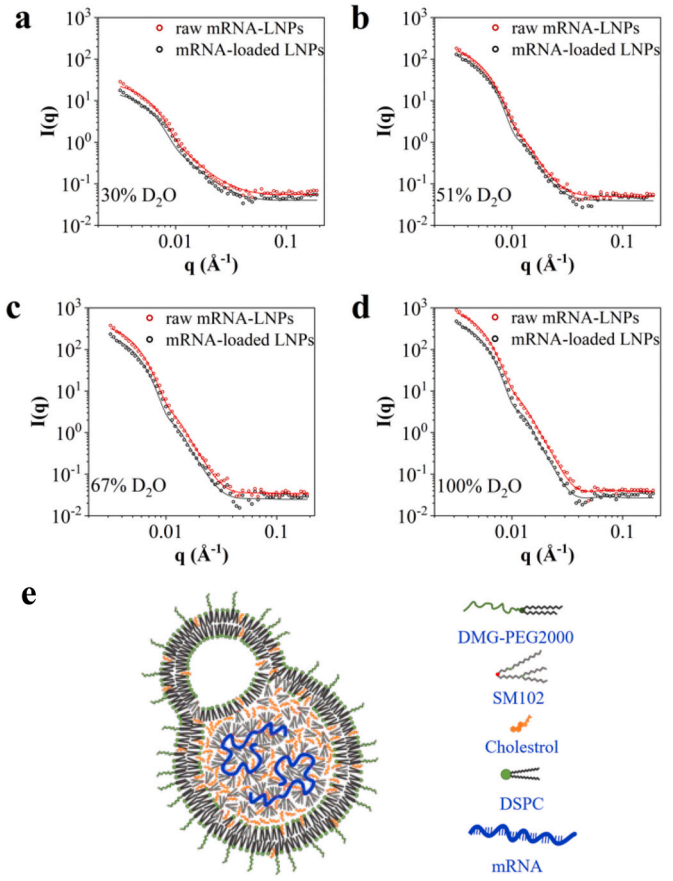

Fig. 5. Structural characterization of mRNA-LNPs by VSANS. VSANS data collected for mRNA-loaded LNPs (black circles) and raw mRNA-LNPs (red circles) in four different solvent contrasts: (a) 30 %, (b) 51 %, (c) 67 %, and (d) 100 % D_2O buffer. Note that our raw mRNA-LNPs contained 70 % mRNA-loaded LNPs and 30 % mRNA-free LNPs, and mRNA-loaded LNPs correspond to the 70 % mRNA-loaded LNPs in the raw mRNA-LNPs. The black and red solid lines are the results of model fitting for the raw mRNA-LNP sample and mRNA-loaded LNPs. (e) The structural model of mRNA-loaded LNPs proposed according to the VSANS fitting results. (For interpretation of the references to colour in this figure legend, the reader is referred to the web version of this article.)

length and lipid composition contribute to variability among the five structural models, the shell thicknesses are comparable across studies, ranging from 6 to 10 nm. Also, the shell thickness and lipid distributions of mRNA-free LNPs and mRNA-loaded LNPs are notably similar. The shell thickness (~7.1 nm) approximates the bilayer thickness of DSPC (5.8 nm) (46), suggesting that a disordered bilayer may form due to the high curvature induced by SM-102. Regarding the lipid composition of our LNP samples, we recognize that the shell structure of LNPs appears to be independent of mRNA encapsulation. Compared to mRNA loading, the lipid distribution in the shell of mRNA-LNPs are more likely to be varied by different lipid compositions, as demonstrated by Arteta et al. (12). Moreover, the lipid distribution within the lipid-rich compartment of the core is comparable between mRNA-free LNPs and mRNA-loaded LNPs, though the core size is larger in mRNA-loaded LNPs. This similarity in lipid distribution is consistent with previous studies (22,47), which demonstrated that changes in mRNA loading exert minimal influence on the lipid distribution of LNPs. Given that mRNA occupies only ~4 % of the volume of the lipid-rich compartment in mRNA-loaded LNPs, we attribute the larger core size to the increased water content introduced by the hydrophilic mRNA molecules. The solvent volume fractions in the lipid-rich compartments of mRNA-free LNPs and mRNA-loaded LNPs are ~3 % and ~ 20 %, respectively. Consequently, we can calculate the densities of cationic ionizable lipids (CILs) in the lipid-rich compartment of the core in mRNA-free LNPs and mRNA-LNPs, which are 0.72 and 0.60 g/cm^3, respectively (see Materials and Methods). Note that the density of CILs in the lipid-rich compartment of the core refers specifically to the compaction of cationic ionizable lipids and does not reflect the total mass density of the LNP. The higher density of CILs in the lipid-rich compartment of the core in mRNA-free LNPs is likely to result in a stronger repulsion between CILs at acidic environment, which may facilitate the rupture of LNP and the fusion between LNP and endosomal membrane. Due to the close correlation between CILs and endosomal escape at acidic pH, we propose that mRNA-free LNPs enhance mRNA-LNP endosomal escape through CIL-mediated membrane fusion and potential secondary effect from proton buffering (48–50). Also, the higher water content in the lipid-rich compartment of the core in mRNA-loaded LNPs could induce stronger osmotic stress during freezing, potentially causing particle rupture and reducing efficacy (51). The higher water content in mRNA-loaded LNPs also increases the likelihood of hydrolysis of both mRNA and cationic ionizable lipids (52–54). Lyophilization, which removes water molecules, may thus offer a promising strategy for the long-term storage of mRNA-LNPs (41,55–57). Overall, the lipid distributions between mRNA-free and mRNA-loaded LNPs are largely consistent, but mRNA-loaded LNPs encapsulate mRNA and more water molecules compared to mRNA-free LNPs.

Furthermore, we sought to determine whether the structural characteristics of mRNA-LNPs can be approximated by characterizing raw mRNA-LNPs. The contrast variation VSANS data for raw mRNA-LNPs were fit using the core-shell ellipsoid model, as depicted in Fig. 5. Notably, most structural parameters between mRNA-loaded LNPs and raw mRNA-LNPs were comparable, with the primary difference observed in the volume fraction of solvent within the lipid-rich compartment of the core (Table 1). Although a slightly smaller core

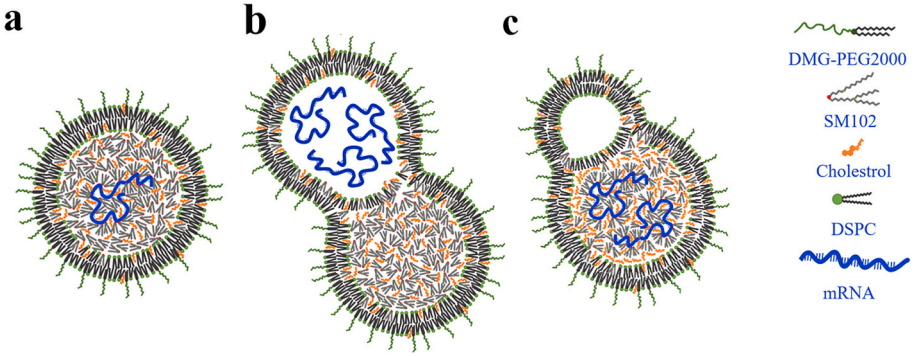

Fig. 6. Sturctural models for mRNA-loaded LNPs. (a) Spherical model proposed by Sebastiani et al. (26), (b) Bleb model with mRNA locates in the water-rich compartment proposed by Cheng et al. (39), and (c) Bleb model with mRNA locates in the lipid-rich compartment proposed in this work.

Table 1
Structure information of mRNA-free LNPs, mRNA-loaded LNPs, and raw mRNA-LNPs determined by VSANS in this work, and structural parameters of the mRNA-LNP samples in Refs. (26) and (27).

Sample[a]		mRNA-free LNPs	mRNA-loaded LNPs	raw mRNA-LNPs	raw mRNA-LNPs	raw mRNA-LNPs
Reference		this work	this work	this work	(26)	(27)
Lipid formulation		CIL:DSPC:Chol:PEGylated lipids = 50:10:38.5:1.5 mol%				
CIL[b]		SM-102	SM-102	SM-102	MC3	SM-102
mRNA length (nt)		0	2856	2856	997	2839
N/P		–	6	6	3	6
Morphology		Bleb	Bleb	Bleb	Sphere	Sphere
R_h (nm)[c]		47.8 ± 2.0	–	63.5 ± 0.6	43 ± 1	–
R_g (nm)[d]		32.8	–	46.1	33	32.3
Nanoparticle volume fraction (v/v%)[e]	core	65.8 ± 1.1	67.3 ± 1.3	67.9 ± 1.2	58 ± 7	32.0 ± 4.8
	shell	34.2 ± 0.7	32.7 ± 0.7	32.1 ± 0.6	42 ± 7	68.0 ± 4.8
Core radius (nm)[f]		30.0 ± 0.1 /36.0 ± 0.1	34.9 ± 0.1 /41.9 ± 0.1	33.5 ± 0.1 /40.2 ± 0.1	28 ± 3	22.1 ± 1.9
Shell thickness (nm)		7.1 ± 0.1	7.0 ± 0.1	6.9 ± 0.1	6 ± 1	10.2 ± 1.2
Total radius (nm)		37.1 ± 0.1 /43.1 ± 0.1	41.9 ± 0.1 /48.9 ± 0.1	40.4 ± 0.1 /47.1 ± 0.1	33 ± 2	32.3 ± 3.1
"dry" volume fraction in lipid-rich compartment of the core (v/v%)	mRNA	0	3.51 ± 0.07	3.48 ± 0.06	13 ± 2	6 ± 1
	CIL	80.3 ± 5.9	78.6 ± 5.1	79.5 ± 1.5	75 ± 1	72 ± 2
	Chol	19.7 ± 5.9	17.9 ± 5.1	17.0 ± 1.5	12 ± 1	21 ± 1
Volume fraction of solvent in lipid-rich compartment of the core (v/v%)		3.1 ± 2.0	20.4 ± 1.6	12.6 ± 0.5	18 ± 5	32 ± 1
Lipid shell "dry" volume fraction (v/v%)	CIL	23.2 ± 5.2	18.9 ± 6.4	27.0 ± 6.6	38 ± 7	61 ± 1
	DSPC	41.3 ± 6.0	43.4 ± 7.7	44.3 ± 7.5	26 ± 4	19 ± 1
	Chol	31.0 ± 5.5	32.9 ± 7.0	23.8 ± 6.4	33 ± 3	16 ± 1
	PEGylated lipids	4.6 ± 1.4	4.8 ± 1.7	4.9 ± 1.7	3.0 ± 0.5	4 ± 1
Volume fraction of solvent in shell (v/v%)		50.0 ± 2.1	52.6 ± 2.5	51.2 ± 2.5	–	32
mRNA copy number per LNP		–	3.2 ± 0.2	3.2 ± 0.2	~30	2.7 ± 0.4

[a] Raw mRNA-LNPs refer to the experimental mRNA-LNP samples, comprising both mRNA-free LNPs and mRNA-loaded LNPs. In contrast, mRNA-loaded LNPs represent mRNA-LNPs isolated from these samples by excluding the contribution of mRNA-free LNPs, containing only mRNA-loaded LNPs.
[b] Abbreviations used include MC3 (*O*-(*Z,Z,Z,Z*-heptatriaconta-6,9,26,29-tetraen-19-yl)-4-(*N,N*-dimethylamino)-butanoate), CIL (cationic ionizable lipid), DSPC (1,2-distearoyl-sn-glycero-3-phosphocholine), and Chol (cholesterol). The N/P ratio refers to the molar ratio of amine groups in the CIL to phosphate groups in mRNA.
[c] Hydrodynamic radius (R_h) was determined by dynamic light scattering (DLS).
[d] Radius of gyration (R_g) was measured via small angle X-ray scattering (SAXS) or small angle neutron scattering (SANS).
[e] The volume fractions were estimated from the fitted scattering length density (SLD) using a core-shell ellipsoid model. In the structural analysis of mRNA-LNPs, the distributions of DSPC and DMG-PEG lipids were fixed within the shell, while mRNA was localized in the core.
[f] Given the bleb morphology of both mRNA-free and mRNA-loaded LNPs, the core and total radii of our samples are expressed as an equatorial radius followed by a polar radius, reflecting their ellipsoidal shape.

size and reduced mRNA volume fraction were observed in the core of raw mRNA-LNPs, these differences were not significant. Given the similarity in lipid distributions between mRNA-free LNPs and mRNA-loaded LNPs, we anticipate that the lipid distribution in raw mRNA-LNPs closely mirrors that of mRNA-loaded LNPs. Notably, the volume fraction of solvent in the lipid-rich compartment of mRNA-loaded LNPs was 20.4 %. In contrast, the volume fraction was only 12.6 % when fitting the VSANS data for raw mRNA-LNPs, suggesting that the solvent content in mRNA-loaded LNPs could be substantially underestimated if the presence of mRNA-free LNPs is ignored. Moreover, we suspect that both the core size and mRNA copy number per LNP may be underestimated if the proportion of mRNA-free LNPs is too high in the raw mRNA-LNP sample. However, the shell thickness and lipid distributions in both core and shell appear independent of mRNA encapsulation, indicating that they can be reliably estimated by characterizing the mixture of mRNA-free LNPs and mRNA-LNPs. These insights allow us to tailor the characterization approach based on the structural parameters of interest. For example, shell thickness and lipid distribution in mRNA-LNPs can be obtained through contrast variation SANS on the mixture of mRNA-free LNPs and mRNA-loaded LNPs. On the other hand, if core size and mRNA payload per LNP are the primary focus, the proportion of mRNA-free LNPs in the sample should be reasonably low. In our case, we suggest that this proportion be kept below approximately 30 %. Importantly, determining the solvent content in mRNA-LNPs is highly sensitive to the amount of mRNA-free LNPs, underscoring the need for simultaneous SANS measurements on both raw mRNA-LNPs and the proportion of mRNA-free LNPs within the mixed sample.

Despite the strengths of our combined strategy, two modeling approximations are necessary to extract meaningful structural information. These include fixing the axial ratio (r_{polar}/r_{equat}) at 1.2 and assuming a spherical lipid-rich compartment. While a small subset of nanoparticles may deviate from these assumptions due to morphological heterogeneity, the approximations are supported by cryo-EM analysis for the majority of particles. The derived structural parameters should be interpreted as ensemble-averaged values, and caution is warranted when considering their absolute accuracy. Nonetheless, the comparative structural trends observed between mRNA-free and mRNA-loaded LNPs remain valid and reproducible. These findings provide new insight into LNP heterogeneity and are expected to inform future structure–function studies in RNA delivery.

4. Conclusion

In summary, we have developed a method for characterizing the structure of mRNA-LNPs in the presence of mRNA-free LNPs by integrating contrast variation SANS and NanoFCM. From the SANS data, we generated a structural model of mRNA-free LNPs. Using NanoFCM, we quantified the proportion of mRNA-free LNPs in our mRNA-LNP sample, which was approximately 30 %. This allowed us to isolate the SANS curves specific to mRNA-loaded LNPs by subtracting the contributions of mRNA-free LNPs from the composite SANS data. As a consequence, we resolved the structural features of mRNA-loaded LNPs within a mixture of mRNA-free LNPs and mRNA-loaded LNPs, proposing an accurate model for mRNA-loaded LNPs. The more accurate structural model of

mRNA-loaded LNPs may shed light on the optimization of formulation due to the close correlation between structure and activity of mRNA-LNP samples (12,25,26).

Additionally, we realized that the lipid distributions and thickness of shell were quite similar by comparing the structural parameters between mRNA-free LNPs and mRNA-loaded LNPs. Therefore, the two structural information can be acquired via SANS, regardless of the amount of mRNA-free LNPs in the sample. In contrary, the solvent content in mRNA-free LNPs is much less than that in mRNA-loaded LNPs. The higher solvent content in mRNA-loaded LNPs also give rise to a larger core size than that of mRNA-free LNPs. However, we note that the core size and mRNA payload per LNP can be approximated by directly characterizing the mRNA-LNP sample only if the proportion of mRNA-free LNPs is not two large, such as less than 30 % in our study. Our methodology not only enables the determination of mRNA-LNP structure in the presence of mRNA-free LNPs, but also establishes a framework for selecting appropriate characterization techniques based on the specific structural parameters of interest.

5. Materials and methods

5.1. Materials

An enhanced green fluorescent protein-linked firefly luciferase (eGFP-fLuc) encoding mRNA with sequence length of 2856 nucleotides, was obtained from Yaohaibio Co., Ltd. (Jiangsu, China). This mRNA was synthesized via in vitro transcription, incorporating a Cap1 structure at the 5′ end, pseudouridine substitutions, and a 150-nucleotide poly(A) tail, with a purity of greater than 95 % for the full-length construct. The cationic ionizable lipid (CIL), heptadecan-9-yl 8-((2-hydroxyethyl)(6-oxo-6-(undecyloxy)hexyl)amino)octanoate (SM102, CAS: 2089251–47-6), was purchased from Sinopeg Biotechnology Co., Ltd. (Fujian, China). 1,2-Distearoyl-sn-glycero-3-phosphocholine (DSPC, CAS: 816–94-4) was sourced from Merck KGaA (Darmstadt, Germany). Cholesterol (Chol, CAS: 57–88-5) and 1,2-Dilauryl-rac-glycero-3-methoxypolyethylene glycol 2000 (DMG-PEG2000, CAS: 160743–62-4) were obtained from Avanti Polar Lipids, Inc. (Alabaster, AL, USA). Trehalose (CAS: 6138-23-4) was purchased from Shaoxin Biotechnology Co., Ltd. (Shanghai, China).

5.2. Sample preparation

mRNA was dissolved in a 100 mM citrate buffer (pH 4.0) at a concentration of 72 μg/mL, serving as the aqueous phase. The lipid mixture, composed of SM-102, cholesterol, DSPC, and DMG-PEG2000 in a molar ratio of 50:38.5:10:1.5, was dissolved in anhydrous ethanol. Both the aqueous and ethanol phases were equilibrated to room temperature prior to use. The raw mRNA-LNP samples were generated using a microfluidic device (NanoGenerator Flex, Precigenome LLC, CA, USA) at a total flow rate of 4 mL/min, with an aqueous-to-organic phase flow rate ratio of 3:1. The initial mixture (~0.25 mL from the first 5 s) was discarded to avoid the effect of non-equilibrium flow and residual buffer in the outlet channel. The primary mRNA-LNP suspension, containing 8 mM lipid and an N:P ratio of 6:1, was immediately diluted tenfold in Tris buffer (pH 7.4) to reduce ethanol concentration and facilitate buffer exchange. Ultrafiltration at 3000 rpm using a 100 kDa MWCO Millipore filter was employed to remove excess buffer. The buffer replacement process was repeated to ensure the final ethanol content was reduced to less than 0.5 %. For subsequent testing, raw mRNA-LNPs at various concentrations were concentrated using ultrafiltration. As a negative control, mRNA-free LNPs were prepared using 100 mM sodium citrate buffer (pH 4.0) as the aqueous phase, following the same lipid composition and formulation protocol as the raw mRNA-LNPs, but without the addition of nucleic acids. A 30 kDa molecular weight cutoff (MWCO) Millipore filter was used for sample purification in the case of mRNA-free LNPs.

5.3. Dynamic light scattering (DLS)

The hydrodynamic radius (R_h) and polydispersity index (PdI) of mRNA-free LNPs and raw mRNA-LNPs were measured using a Nano-Brook Omni multi-angle particle size and zeta potential analyzer (Brookhaven Instruments, NH, USA). Prior to measurement, 25 μL of the LNP samples was diluted with 500 μL of DEPC water and placed in a 50 μL disposable plastic cuvette (Brookhaven). Measurements were conducted at a scattering angle of 90° using a 640 nm laser and with the dust filter enabled. The refractive index of the particles was set to 1.45, following Ref. (12). Samples were equilibrated at 25 °C for 120 s before measurement. The apparent hydrodynamic diameter was determined using the Einstein-Stokes equation and is reported as the radius of an equivalent spherical particle.

5.4. Cryogenic electron microscopy (cryo-EM)

The morphology of mRNA-free LNPs and raw mRNA-LNPs was examined using cryogenic electron microscopy (cryo-EM). Sample preparation was conducted with a Leica EM GP2 automatic plunge freezer (Wetzlar, Germany). Briefly, 3 μL of the LNP suspension, at a lipid concentration of 5–10 mg/mL, was applied to a plasma-cleaned lacey copper grid coated with a continuous carbon film. Excess sample was blotted without damaging the carbon layer. The grids were then stored in liquid nitrogen prior to imaging. For the stained sample, 3 μL of 0.1 mM thionine acetate was applied immediately before flash-freezing for cryo-EM. Cryo-EM imaging was performed on a Talos F200C G2 Microscope (Thermo Fisher Scientific, MA, USA) operated at 200 kV, utilizing a Schottky thermal field emission super-bright electron gun. During imaging, sample grids were maintained below −170 °C. Images were captured using a FEI Ceta 4 k × 4 k camera, with acquisition facilitated by EPU and Serial EM software.

5.5. Encapsulation efficiency

The encapsulation efficiency (EE%) of our mRNA-LNP sample was determined using the Quant-iT RiboGreen RNA Quantification Kit, following the manufacturer's protocol, in a black 96-well plate. In brief, 1 μL of mRNA-LNP suspension was diluted in 100 μL of Tris-EDTA (TE) buffer for free mRNA measurement or TE buffer containing 2 % Triton X-100 for total mRNA measurement. Encapsulated mRNA was not accessible to RiboGreen, whereas Triton X-100 disrupted the LNPs, releasing the mRNA. Subsequently, 100 μL of a 2000-fold or 200-fold diluted RiboGreen solution was added to the respective wells containing the free or total mRNA solutions. RiboGreen fluorescence, which intensifies upon binding to nucleic acids, was measured at 525 nm (excitation at 425 nm) using a Spark multimode microplate reader (Tecan, Männedorf, Switzerland). Calibration curves, ranging from 0 to 100 ng/mL and 0 to 2000 ng/mL of mRNA, were prepared by serial dilutions and mixed with the corresponding RiboGreen solutions in the same plate. Free and total mRNA concentrations were calculated from the calibration curves, and encapsulation efficiency (EE%) was calculated using the formula:

$$EE\% = \left(1 - \frac{C_{free}}{C_{total}}\right) \times 100\% \quad (1)$$

where C_{total} represents the total mRNA concentration in the presence of 2 % Triton X-100, and C_{free} represents the free (unencapsulated) mRNA concentration.

5.6. In vitro activity

HEK293T cells (Human Embryonic Kidney 293 Cells transformed with sheared Simian Virus 40 Large T Antigen) were obtained from the Cell Resource Center of the Chinese Academy of Sciences (Shanghai, China) and cultured following the manufacturer's protocols. Cells were

maintained in high-glucose Dulbecco's Modified Eagle Medium (DMEM, Thermo Fisher Scientific, CA, USA) supplemented with 10 % fetal bovine serum (FBS, Gibco, Australia) and 1 % penicillin/streptomycin, and incubated at 37 °C in a 5 % CO_2 atmosphere. Third-passage cells, at a density of 3×10^5 cells/mL, were seeded into 24-well plates (500 μL per well) and allowed to adhere for 24 h prior to transfection. For transfection, 20 μL of mRNA-LNP suspension containing ~1 μg mRNA was added dropwise to each well in triplicate, followed by a 24-h incubation. The expression of mRNA in HEK293T cells was assessed by measuring firefly luciferase activity using the Firefly Luciferase Reporter Gene Assay Kit (Beyotime Biotechnology, Shanghai, China) as per the manufacturer's instructions. After removing the culture medium, 100 μL of cell lysis buffer was added to each well, and the cell lysates were centrifuged at 10,000 ×*g* for 5 min. A 40 μL aliquot of the supernatant was mixed with 100 μL of Firefly Luciferase Assay Reagent, and luminescence (RLU) was measured using a SpectraMax iD5 multi-mode microplate reader (Becton, Dickinson and Company, NJ, USA). The RLU values were normalized to the amount of encapsulated mRNA, quantified by the Quant-iT RiboGreen RNA Quantification Kit, and reported as normalized RLU (Norm RLU).

5.7. Nano flow cytometry (NanoFCM)

The payload and capacity of mRNA-LNPs were quantified using a Flow NanoAnalyzer (NanoFCM Inc., Fujian, China). The mRNA-LNP suspension was serially diluted to achieve particle concentrations between 1×10^8 to 1×10^{10} particles/mL in buffer solutions. These dilutions were manually processed and analyzed by the Flow NanoAnalyzer. SYTO 9, a green fluorescent nucleic acid stain (Invitrogen, Thermo Fisher Scientific, MA, USA), was added to the diluted samples and incubated at 37 °C for 15 min prior to analysis. Subsequently, 100 μL of the stained sample was loaded into the analyzer to assess particle concentration, the proportion of mRNA-free LNPs, and the payload of mRNA within the LNPs. To validate the accuracy and specificity of the nano flow cytometry–based quantification method, both mRNA-free LNPs and free mRNA in aqueous solution samples are measured by using the same procedure as raw mRNA-LNPs (see Fig. S6). Quantitatively, the proportion of false-positive events—defined as fluorescent signals in mRNA-free LNPs—was only 2.3 %, which is within the noise level and considered negligible. These findings confirm the specificity of the SYTO 9-based staining method and support its reliability for distinguishing mRNA-loaded from mRNA-free LNPs. Thus, both control experiments—using mRNA-free LNPs and free mRNA—help validate the accuracy and specificity of the nano flow cytometry–based quantification method employed in this study.

5.8. Small angle X-ray scattering (SAXS)

SAXS measurements were conducted at the BL19U2 beamline of the Shanghai Synchrotron Radiation Facility (SSRF) using a synchrotron X-ray source with a wavelength of 0.103 nm. The experimental setup included a Pilatus 2 M detector (172 μm × 172 μm pixel size), offering a resolution of 1043 × 981 pixels. The sample-to-detector distance was set to 2.6 m, allowing for a scattering vector range (q) from 0.006 $Å^{-1}$ to 0.3 $Å^{-1}$. SAXS measurements were performed on three sample types: (1) mRNA-free LNPs (1.25 mg/mL total lipid concentration in Tris-HCl, pH 7.4), (2) raw mRNA-LNPs (1.25 mg/mL lipid containing 54 μg/mL mRNA in Tris buffer), and (3) free mRNA in aqueous solution (54 μg/mL in citrate buffer, pH 4.0). Each 100 μL sample were loaded into an annular cell with Kapton windows separated by a Teflon spacer. Twenty consecutive two-dimensional (2D) SAXS images were recorded with an exposure time of 0.5 s per frame. The resulting images were integrated into one-dimensional (1D) intensity curves using BioXTAS RAW 2.3.0 software (58). The intensity curves were averaged across all 20 frames, and solvent background subtraction was performed to obtain the final data.

5.9. Small angle neutron scattering (SANS)

SANS experiments were conducted using both the Small Angle Neutron Scattering (SANS) instrument BL-01 (59) and the Very Small Angle Neutron Scattering (VSANS) instrument BL-14 (60) at the China Spallation Neutron Source (CSNS). The SANS data were collected in a q range of 0.005 to 0.6 $Å^{-1}$, with a sample-to-detector distance of 4 m and neutron wavelengths ranging from 1 Å to 12 Å. The VSANS data were collected in a q range of 0.003 to 0.2 $Å^{-1}$, neutron wavelengths ranging from 6 Å to 10.5 Å. LNP samples, diluted to a final concentration of 3 mg/mL in a solvent mixture of D_2O and H_2O, were placed in quartz cells with a 2 mm optical path length. Measurement durations varied from 0.5 to 3 h, based on the scattering intensity. All experiments were conducted at 298 K. The SANS data presented were background-subtracted (solvent), corrected for empty cell contributions, and adjusted for transmission.

5.10. Data analysis of SAXS

The scattering pattern of a particle $I(q)$ is a Fourier transform of its pair distance distribution function, P(r), being related to each other by the equation (61):

$$P(r) = \frac{r^2}{2\pi^2}\int_0^\infty \frac{q^2 I(q)\sin(qr)}{qr} dq \tag{2}$$

where r is the pair distance in real space, and q is the momentum transfer in reciprocal space. Furthermore, the radius of gyration (R_g) can be calculated from the $P(r)$ function using the Eq. (61):

$$R_g^2 = \frac{\int_0^{D_{max}} r^2 P(r) dr}{2\int_0^{D_{max}} P(r) dr} \tag{3}$$

where D_{max} is the maximum dimension of the particle.

5.11. Data analysis of SANS

The analysis of Small Angle Neutron Scattering (SANS) and Very Small Angle Neutron Scattering (VSANS) data was performed using SasView software (https://www.sasview.org/). Both the SANS and VSANS instruments provide a specific data column indicating the resolution smearing at each q. Accordingly, we used the SasView software to fit the SANS and VSANS data with instrumental resolution smearing explicitly incorporated. The lipid composition of the lipid nanoparticles (LNPs) was determined using samples with a lipid molar ratio of SM-102:DSPC:Chol:DMG-PEG2000 of 50:10:38.5:1.5, incorporating deuterated d70-DSPC and d7-Chol. The VSANS profile of the mRNA-loaded LNPs was derived by accounting for the estimated proportion of mRNA-free particles (~30 %) in the raw mRNA-LNP sample, using the following equation:

$$I_{(raw\ mRNA-LNPs)}(q) = 70\% \times I_{(mRNA-loaded\ LNPs)}(q) + 30\% \times I_{(mRNA-free\ LNPs)}(q) \tag{4}$$

where $I_{(raw\ mRNA-LNPs)}(q)$, $I_{(mRNA-loaded\ LNPs)}(q)$, and $I_{(mRNA-free\ LNPs)}(q)$ are the VSANS intensity of raw mRNA-LNPs, mRNA-loaded LNPs, and mRNA-free LNPs at the scattering wavevector q, respectively. The VSANS data were fitted using a core-shell ellipsoid model (44), with shell thickness constrained to be isotropic and the ratio of the equatorial to polar radius fixed at 1.2 based on cryo-EM images of mRNA-free LNPs and mRNA-LNPs (Fig. 1b). Therefore, four independent parameters, including the equatorial radius of the core (r_{equat}), the shell thickness (t_{shell}), the scattering length density of the core (SLD_{core}), and the scattering length density of the shell (SLD_{shell}) (see Fig. 2), were determined by the curve fitting. The fitting was conducted over a q range of 0.003 $Å^{-1}$ to 0.2 $Å^{-1}$.

The following parameters were estimated and fixed:

(i) The scale factor and background were individually determined for each dataset.
(ii) The solvent scattering length density (SLD) was calculated based on the D_2O/H_2O ratio used, referencing the SLDs of D_2O and H_2O (Table S1).
(iii) Polydispersity, characterized by the Schulz distribution, was estimated from the data and fixed across all solvent contrasts.

The fitting parameters included:

(i) Constrained radii and thickness, fitted simultaneously across all solvent contrasts.
(ii) Shell and core SLDs, fitted simultaneously for each solvent contrast.

Table S2 presents the fitting parameters for the VSANS data of mRNA-free LNPs, and raw and mRNA-loaded LNPs. For structural resolution of the core, the SLD of the lipid-rich compartment of the core was calculated using the formula:

$$SLD_{core} = vf_{water-rich} \times SLD_{solv} + vf_{lipid-rich} \times SLD_{lipid-rich} \quad (5)$$

where SLD_{core} is the SLD of the core, SLD_{solv} is the SLD of the solvent, $SLD_{lipid-rich}$ is the SLD of the lipid-rich compartment of the core, $vf_{water-rich}$ is the volume fraction of the water-rich compartment of the core, and $vf_{lipid-rich}$ is the volume fraction of the lipid-rich compartment of the core. We approximated the lipid-rich compartment inside the core to be spherical such that the volume fractions of water-rich and lipid-rich compartments in the core are 0.2/1.2 and 1/1.2, respectively (see Fig. 2).

The volume fraction of solvent and the dry SLD of the shell and the lipid-rich compartment of the core were derived from the fitted wet SLDs:

$$SLD_{lipid-rich} = \left(1 - vf_{solv\_in\_lipid-rich}\right) \times SLD_{dry\_lipid-rich} + vf_{solv\_in\_lipid-rich} \times SLD_{solv} \quad (6)$$

$$SLD_{shell} = \left(1 - vf_{solv\_in\_shell}\right) \times SLD_{dry\_shell} + vf_{solv\_in\_shell} \times SLD_{solv} \quad (7)$$

where $vf_{solv\_in\_lipid-rich}$ is the volume fraction of solvent in the lipid-rich compartment of the core, $SLD_{dry\_lipid-rich}$ is the dry SLD of the lipid-rich compartment of the core, SLD_{solv} is calculated for each contrast as detailed in Table S1, SLD_{shell} is the SLD of shell, $vf_{solv\_in\_shell}$ is the volume fraction of solvent in the shell, and SLD_{dry_shell} is the dry SLD of the shell. The calculated dry SLDs and solvent volume fractions for the lipid-rich compartment and the shell are reported as the mean of these calculated values, with standard deviations indicating the error.

The lipid composition of lipid-rich compartment and shell was determined using the method outlined by Sebastiani et al. (25). This method partitions the molecules between shell and core based on molecular volumes and available volumes. The calculated SLDs were matched to the fitted SLDs to determine the volume fractions, which were then converted to molar fractions using component molecular volumes. The calculations assume the conservation of the input lipid molar ratio and consider the encapsulation efficiency as measured by the RiboGreen assay. All DSPC and PEG lipids were assumed to be in the shell, and all mRNA was assumed to be in the lipid-rich compartment of the core. The conversion from SLD to volume fraction and subsequently to molar fraction is described as follows:

From SLD to volume fraction:

$$vf_{x,i} = \frac{V_i}{V_{x,LNP}} \quad (8)$$

where i is any of the LNP components including the solvent, and x is either lipid-rich or shell.

$$SLD_{lipid-rich} = \sum_i vf_{lipid-rich,i} SLD_i \quad (9)$$

$$SLD_{shell} = \sum_i vf_{shell,i} SLD_i \quad (10)$$

From volume fraction to molar fraction:

$$\text{Molar fraction of component } x \; F_{M,x} = \frac{N_{M,x}}{N_{total}} \quad (11)$$

$$\text{Volume fraction of component } x \;\; F_{v,x} = \frac{V_{M,x}}{V_{total}} \quad (12)$$

$$\text{Number of moles of component x } N_{M,x} = \frac{V_{M,x}}{V_{mol,x}} \quad (13)$$

$$\text{Total number of moles } N_{total} = \sum_i \frac{V_{M,i}}{V_{mol,i}} = \sum_i \frac{F_{v,i} V_{total}}{V_{mol,i}} = V_{total} \sum_i \frac{F_{v,i}}{V_{mol,i}} \quad (14)$$

$$\text{Molar fraction of component } F_{M,x} = \frac{V_{M,x}}{V_{mol,x} V_{total} \sum_i \frac{F_{v,i}}{V_{mol,i}}} = F_{v,x} \frac{1}{V_{mol,x} \sum_i \frac{F_{v,i}}{V_{mol,i}}} \quad (15)$$

5.11.1. Calculation of the density of CILs in the lipid-rich compartment of the core

According to the fitting results in Table 1, we can calculate the densities of CILs in the lipid-rich compartment of the core in both mRNA-free LNPs and mRNA-loaded LNPs:

$$\rho_{CILs\_in\_lipid-rich} = \left(\rho_{CILs} * \frac{vf_{dry\_CILs}}{vf_{dry\_CILs} + vf_{dry\_chol} + vf_{dry\_mRNA} + vf_{solv\_in\_lipid-rich}} * V_{lipid-rich} \right) \Big/ V_{lipid-rich} \quad (16)$$

where ρ_{CILs} is the density of CILs, $V_{lipid-rich}$ is the volume of the lipid-rich compartment of the core, $vf_{solv\_in\_lipid-rich}$ is the volume fraction of solvent in the lipid-rich compartment of the core, and vf_{dry_CILs}, vf_{dry_chol}, and vf_{dry_mRNA} are the volume fractions of CILs, cholesterol, and mRNA in the dry lipid-rich compartment of the core, respectively. The density of SM-102 used in this work is 0.925 g/cm^3.

CRediT authorship contribution statement

Xiaoxia Chen: Writing – review & editing, Writing – original draft, Methodology, Investigation, Formal analysis, Data curation. **Yongfeng Ye:** Methodology, Formal analysis, Data curation. **Mengrong Li:** Validation, Investigation. **Taisen Zuo:** Methodology. **Zhenhua Xie:** Methodology. **Yubin Ke:** Methodology. **He Cheng:** Methodology. **Liang Hong:** Writing – review & editing, Supervision, Funding acquisition, Conceptualization.**Zhuo Liu:** Writing – review & editing, Writing – original draft, Validation, Supervision, Project administration, Methodology, Investigation, Funding acquisition, Formal analysis, Data

curation, Conceptualization.

Declaration of competing interest

The authors declare no competing financial interest.

Acknowledgements

This work was supported by the National Natural Science Foundation of China (12204302), the Natural Science Foundation of Shanghai (Grant No. 23ZR1431700), and the Student Innovation Center at Shanghai Jiao Tong University. We thank the staff members of BL19U2 beamline (https://cstr.cn/31129.02.NFPS.BL19U2) at the National Facility for Protein Science in Shanghai (https://cstr.cn/31129.02.NFPS), for providing technical support and assistance in data collection and analysis. This work was previously made available as a bioRxiv preprint (doi: https://doi.org/10.1101/2024.09.27.614859).

Appendix A. Supplementary data

Supplementary data to this article can be found online at https://doi.org/10.1016/j.jconrel.2025.114082.

Data availability

Data will be made available on request.

References

[1] Y. Zhu, et al., Screening for lipid nanoparticles that modulate the immune activity of helper T cells towards enhanced antitumour activity, Nat. Biomed. Eng. (2023), https://doi.org/10.1038/s41551-023-01131-0.
[2] L. Miao, et al., Delivery of mRNA vaccines with heterocyclic lipids increases anti-tumor efficacy by STING-mediated immune cell activation, Nat. Biotechnol. 37 (2019) 1174–1185.
[3] N. Matharu, et al., CRISPR-mediated activation of a promoter or enhancer rescues obesity caused by haploinsufficiency, Science 363 (2019) eaau0629.
[4] B. Truong, et al., Lipid nanoparticle-targeted mRNA therapy as a treatment for the inherited metabolic liver disorder arginase deficiency, Proc. Natl. Acad. Sci. U. S. A. 116 (2019) 21150–21159.
[5] L.R. Baden, et al., Efficacy and safety of the mRNA-1273 SARS-CoV-2 vaccine, N. Engl. J. Med. 384 (2020) 403–416.
[6] F.P. Polack, et al., Safety and efficacy of the BNT162b2 mRNA Covid-19 vaccine, N. Engl. J. Med. 383 (2020) 2603–2615.
[7] R. Tenchov, R. Bird, A.E. Curtze, Q. Zhou, Lipid nanoparticles—from liposomes to mRNA vaccine delivery, a landscape of research diversity and advancement, ACS Nano 15 (2021) 16982–17015.
[8] X. Hou, T. Zaks, R. Langer, Y. Dong, Lipid nanoparticles for mRNA delivery, Nat. Rev. Mater. 6 (2021) 1078–1094.
[9] N.-N. Zhang, et al., A thermostable mRNA vaccine against COVID-19, Cell 182 (2020) 1271–1283.e16.
[10] L. Zheng, S.R. Bandara, Z. Tan, C. Leal, Lipid nanoparticle topology regulates endosomal escape and delivery of RNA to the cytoplasm, Proc. Natl. Acad. Sci. U. S. A. 120 (2023) e2301067120.
[11] S. Patel, et al., Naturally-occurring cholesterol analogues in lipid nanoparticles induce polymorphic shape and enhance intracellular delivery of mRNA, Nat. Commun. 11 (2020) 983.
[12] M. Yanez Arteta, et al., Successful reprogramming of cellular protein production through mRNA delivered by functionalized lipid nanoparticles, Proc. Natl. Acda. Sci. U. S. A. 115 (2018) E3351–E3360.
[13] J. Viger-Gravel, et al., Structure of lipid nanoparticles containing siRNA or mRNA by dynamic nuclear polarization-enhanced NMR spectroscopy, J. Phys. Chem. B 122 (2018) 2073–2081.
[14] J.A. Kulkarni, et al., On the formation and morphology of lipid nanoparticles containing Ionizable cationic lipids and siRNA, ACS Nano 12 (2018) 4787–4795.
[15] A.K.K. Leung, et al., Lipid nanoparticles containing siRNA synthesized by microfluidic mixing exhibit an Electron-dense nanostructured Core, J. Phys. Chem. C 116 (2012) 18440–18450.
[16] A. Henrickson, et al., Density matching multi-wavelength analytical ultracentrifugation to measure drug loading of lipid nanoparticle formulations, ACS Nano 15 (2021) 5068–5076.
[17] A. Kamanzi, et al., Simultaneous, single-particle measurements of size and loading give insights into the structure of drug-delivery nanoparticles, ACS Nano 15 (2021) 19244–19255.
[18] M.L. Brader, et al., Encapsulation state of messenger RNA inside lipid nanoparticles, Biophys. J. 120 (2021) 2766–2770.
[19] J. Szebeni, et al., Insights into the structure of Comirnaty Covid-19 vaccine: a theory on soft, partially bilayer-covered nanoparticles with hydrogen bond-stabilized mRNA–lipid complexes, ACS Nano 17 (2023) 13147–13157.
[20] S. Li, et al., Payload distribution and capacity of mRNA lipid nanoparticles, Nat. Commun. 13 (2022) 5561.
[21] Z. Li, et al., Acidification-induced structure evolution of lipid nanoparticles correlates with their in vitro gene transfections, ACS Nano 17 (2023) 979–990.
[22] J. Gilbert, et al., Evolution of the structure of lipid nanoparticles for nucleic acid delivery: from in situ studies of formulation to colloidal stability, J. Colloid Interface Sci. 660 (2024) 66–76.
[23] M.M. Wang, et al., Elucidation of lipid nanoparticle surface structure in mRNA vaccines, Sci. Rep. 13 (2023) 16744.
[24] T. Unruh, et al., Mesoscopic structure of lipid nanoparticle formulations for mRNA drug delivery: Comirnaty and drug-free dispersions, ACS Nano 18 (2024) 9746–9764.
[25] Y. Fan, et al., Physicochemical and structural insights into lyophilized mRNA-LNP from lyoprotectant and buffer screenings, J. Control. Release 373 (2024) 727–737.
[26] F. Sebastiani, et al., Apolipoprotein E binding drives structural and compositional rearrangement of mRNA-containing lipid nanoparticles, ACS Nano 15 (2021) 6709–6722.
[27] Y. Li, et al., Morphology evolution of lipid nanoparticle discovered by small angle neutron scattering, Giant 20 (2024) 100329.
[28] J. Philipp, et al., pH-dependent structural transitions in cationic ionizable lipid mesophases are critical for lipid nanoparticle function, Proc. Natl. Acad. Sci. U. S. A. 120 (2023) e2310491120.
[29] M.F.W. Trollmann, R.A. Böckmann, mRNA lipid nanoparticle phase transition, Biophys. J. 121 (2022) 3927–3939.
[30] R. Pattipeiluhu, et al., Liquid crystalline inverted lipid phases encapsulating siRNA enhance lipid nanoparticle mediated transfection, Nat. Commun. 15 (2024) 1303.
[31] J. Dawidowski, J.R. Granada, J.R. Santisteban, F. Cantargi, L.A.R. Palomino, Appendix - neutron scattering lengths and cross sections, in: F. Fernandez-Alonso, D.L. Price (Eds.), Experimental Methods in the Physical Sciences vol. 44, Academic Press, 2013, pp. 471–528.
[32] J.L. Thelen, et al., Morphological characterization of self-amplifying mRNA lipid nanoparticles, ACS Nano 18 (2024) 1464–1476.
[33] S. Zhu, et al., Light-scattering detection below the level of single fluorescent molecules for high-resolution characterization of functional nanoparticles, ACS Nano 8 (2014) 10998–11006.
[34] T. Sych, et al., High-throughput measurement of the content and properties of nano-sized bioparticles with single-particle profiler, Nat. Biotechnol. 42 (2024) 587–590.
[35] R. Münter, J.B. Larsen, T.L. Andresen, The vast majority of nucleic acid-loaded lipid nanoparticles contain cargo, J. Colloid Interface Sci. 674 (2024) 139–144.
[36] J.B. Simonsen, A perspective on bleb and empty LNP structures, J. Control. Release 373 (2024) 952–961.
[37] C. Geng, et al., A preparation method for mRNA-LNPs with improved properties, J. Control. Release 364 (2023) 632–643.
[38] A.K.K. Leung, Y.Y.C. Tam, S. Chen, I.M. Hafez, P.R. Cullis, Microfluidic mixing: a general method for encapsulating macromolecules in lipid nanoparticle systems, J. Phys. Chem. B 119 (2015) 8698–8706.
[39] M.H.Y. Cheng, et al., Induction of bleb structures in lipid nanoparticle formulations of mRNA leads to improved transfection potency, Adv. Mater. 35 (2023) 2303370.
[40] J.A. Kulkarni, et al., Fusion-dependent formation of lipid nanoparticles containing macromolecular payloads, Nanoscale 11 (2019) 9023–9031.
[41] S. Meulewaeter, et al., Continuous freeze-drying of messenger RNA lipid nanoparticles enables storage at higher temperatures, J. Control. Release 357 (2023) 149–160.
[42] R. Verbeke, M.J. Hogan, K. Loré, N. Pardi, Innate immune mechanisms of mRNA vaccines, Immunity 55 (2022) 1993–2005.
[43] Y. Lee, M. Jeong, J. Park, H. Jung, H. Lee, Immunogenicity of lipid nanoparticles and its impact on the efficacy of mRNA vaccines and therapeutics, Exp. Mol. Med. 55 (2023) 2085–2096.
[44] S.S. Berr, Solvent isotope effects on alkytrimethylammonium bromide micelles as a function of alkyl chain length, J. Phys. Chem. 91 (1987) 4760–4765.
[45] O. Tirosh, Y. Barenholz, J. Katzhendler, A. Priev, Hydration of polyethylene glycol-grafted liposomes, Biophys. J. 74 (1998) 1371–1379.
[46] A.V. Hughes, et al., Floating lipid bilayers deposited on chemically grafted phosphatidylcholine surfaces, Langmuir 24 (2008) 1989–1999.
[47] S. Liao, et al., Transfection potency of lipid nanoparticles containing mRNA depends on relative loading levels, ACS Appl. Mater. Interfaces 17 (2025) 3097–3105.
[48] S. Chatterjee, E. Kon, P. Sharma, D. Peer, Endosomal escape: a bottleneck for LNP-mediated therapeutics, Proc. Natl. Acda. Sci. U. S. A. 121 (2024) e2307800120.
[49] G. Tesei, et al., Lipid shape and packing are key for optimal design of pH-sensitive mRNA lipid nanoparticles, Proc. Natl. Acda. Sci. U. S. A. 121 (2024) e2311700120.
[50] M. Grau, E. Wagner, Strategies and mechanisms for endosomal escape of therapeutic nucleic acids, Curr. Opin. Chem. Biol. 81 (2024) 102506.
[51] P. Zhao, et al., Long-term storage of lipid-like nanoparticles for mRNA delivery, Bioact. Mater. 5 (2020) 358–363.
[52] M. Packer, D. Gyawali, R. Yerabolu, J. Schariter, P. White, A novel mechanism for the loss of mRNA activity in lipid nanoparticle delivery systems, Nat. Commun. 12 (2021) 6777.
[53] L. Schoenmaker, et al., mRNA-lipid nanoparticle COVID-19 vaccines: structure and stability, Int. J. Pharm. 601 (2021) 120586.
[54] E. Oude Blenke, et al., The storage and in-use stability of mRNA vaccines and therapeutics: not a cold case, J. Pharm. Sci. 112 (2023) 386–403.

[55] H. Muramatsu, et al., Lyophilization provides long-term stability for a lipid nanoparticle-formulated, nucleoside-modified mRNA vaccine, Mol. Ther. 30 (2022) 1941–1951.
[56] L. Ai, et al., Lyophilized mRNA-lipid nanoparticle vaccines with long-term stability and high antigenicity against SARS-CoV-2, Cell Discov. 9 (2023) 9.
[57] M. Li, et al., Lyophilization process optimization and molecular dynamics simulation of mRNA-LNPs for SARS-CoV-2 vaccine, npj Vaccines 8 (2023) 153.
[58] J. Hopkins, BioXTAS RAW 2: new developments for a free open-source program for small-angle scattering data reduction and analysis, J. Appl. Cryst. 57 (2024) 194–208.
[59] Y. Ke, et al., The time-of-flight small-angle neutron spectrometer at China spallation neutron source, Neutron News 29 (2018) 14–17.
[60] T. Zuo, et al., The multi-slit very small angle neutron scattering instrument at the China spallation neutron source, J. Appl. Cryst. 57 (2024) 380–391.
[61] I.S. Dmitri, H.J.K. Michel, Small-angle scattering studies of biological macromolecules in solution, Rep. Prog. Phys. 66 (2003) 1735.